energy&fuels

ARTICLE

pubs.acs.org/EF

# Numerical Study Comparing the Combustion and Emission Characteristics of Biodiesel to Petrodiesel

S. Som* and D. E. Longman

Energy Systems Division, Argonne National Laboratory, 9700 South Cass Avenue, Argonne, Illinois 60439, United States

**ABSTRACT:** Combustion and emission characteristics of compression ignition engines strongly depend upon inner-nozzle flow and spray behavior. These processes control the fuel−air mixing, which in turn is critical for the combustion process. Previous studies by us highlighted the differences in the physical and chemical properties of petrodiesel and biodiesel, which significantly altered the inner-nozzle flow and spray structure. The current study is another step in this direction to gain a fundamental understanding on the influence of fuel properties on the combustion and emission characteristics of the compression ignition engine. *n*-Heptane and methyl butanoate were selected as surrogates for diesel and biodiesel fuels, respectively, because the chemical kinetic pathways were well-understood. Liquid length and flame lift-off length for diesel and biodiesel fuels were validated against data available in the literature. Liquid lengths were always higher for biodiesel because of its higher heat of vaporization, which resulted in increased interplay between spray and combustion processes under all conditions investigated. Ambient air entrainment was also lower for biodiesel mainly because of slower atomization and breakup. The mechanism for flame stabilization is further analyzed by estimating the turbulent burning velocity for both of the fuels. This analysis revealed that neither flame propagation nor isolated ignition kernels upstream and detached from high-temperature regions can be the mechanism for flame stabilization. Flame propagation speeds were observed to be similar for both fuels. Biodiesel predicted lower soot concentrations, which were also reflected in reduced $C_2H_2$ mole fractions. Although prompt $NO_x$ was higher for biodiesel, total $NO_x$ was lower because of reduced thermal $NO_x$. The ignition delay and $NO_x$ emissions predicted by these simulations do not agree with trends reported in the literature; hence, this study highlights the need for better fuel surrogates for diesel and biodiesel fuels.

## 1. INTRODUCTION

Energy security and environmental concerns have stimulated worldwide interest in biologically derived alternative fuels. Biodiesel presents a lucrative alternative, particularly for compression ignition (CI) engines, because it is a renewable energy source that can be used in these engines without significant changes in their design. Modern CI engines can operate with a 5−10% addition of biodiesel by volume, without any loss in performance. Thus, even using biodiesel as an additive can prolong the use of petrodiesel. Biodiesel can be produced from a variety of feedstocks, generally through the transesterification process using an alcohol. There have been several experimental studies on the combustion and emission characteristics of biodiesel and bio-/petrodiesel blends.[1−5] These studies have concluded that biodiesel is environmentally cleaner than petrodiesel (also know as "diesel") with respect to unburnt hydrocarbon (UHC), particulate matter (PM), CO, $CO_2$, and sulfur oxide emissions. In addition, biodiesel also improves the cetane number (CN) and lubrication characteristics. Major drawbacks of biodiesel include increased $NO_x$ production, unfavorable cold-flow properties, and lower energy content.

Further use of biodiesel for CI engine applications can be facilitated by better understanding of its autoignition and emission characteristics. Biodiesel from any feedstock (e.g., soy, rapeseed, tallow, etc.) consists of long-chain oxygenated compounds, such as methyl palmitate, methyl stearate, methyl oleate, and methyl linolenate, in varying proportions. Single droplet ignition delay experiments were performed by Vaughn et al.[6] using different methyl esters, and results were compared against soy biodiesel. Methyl decanoate showed a shorter ignition delay, while methyl oleate captured the ignition delay times accurately compared to biodiesel. The kinetics of oxidation of rapeseed methyl ester (RME) were studied using a jet-stirred reactor (JSR), and intermediate species, stable product concentrations were measured.[7]Because the chemical kinetics of biodiesel components are rather complex, surrogates, such as methyl butanoate (MB),[8] methyl heptanoate, methyl decanoate,[9] methyl oleate,[10] etc., have been studied in shock-tube, rapid-compression machines and with a JSR to understand the influence of ambient conditions, such as temperature, pressure, and the equivalence ratio, on the chemical ignition delay times.

Detailed combustion simulations of biodiesel can be performed with reliable reduced mechanisms for biodiesel surrogates. Although several surrogate fuels for biodiesel have been proposed, the lack of reduced mechanisms inhibits their use for CI engine modeling. Brakora et al.[11] developed a reduced mechanism using MB as a surrogate for biodiesel, which consists of 41 species and 150 reactions. While performing CI engine simulations using KIVA, they assumed that the injection characteristics would be similar for diesel and biodiesel fuels, which may not be an accurate assumption. The mechanism successfully

**Received:** September 13, 2010
**Revised:** March 2, 2011
**Published:** March 04, 2011

ACS Publications © 2011 American Chemical Society

predicted ignition timing, pressure, and heat-release-rate characteristics. Using the same biodiesel surrogate, Ra et al.[12] performed parametric studies to investigate the effects of various physical properties on combustion characteristics. They observed that the results were most sensitive to liquid density, vapor pressure, and surface tension. Golovitchev and Yang[13] developed a kinetic model for RME with MB as a surrogate fuel. The reduced mechanism consisted of 88 species and 363 reactions and was validated against shock-tube and flame speed data. CI engine simulations were also performed. Um and Park[14] developed a kinetic model for biodiesel derived from rice oil with a mixture of MB and *n*-heptane (NHPT) as a surrogate. Simulations captured the CO and hydrocarbon (HC) emissions well for different blends of diesel and biodiesel. However, $NO_x$ emissions were not accurately predicted.

The literature search identified relatively few studies dealing with fundamental combustion and emission characteristics of biodiesel fuels. These characteristics of a conventional CI engine are strongly coupled with the flame lift-off behavior, as demonstrated by several previous studies.[15−20] While the flame lift-off characteristics of diesel fuel and its surrogates (such as NHPT) have been investigated in great detail, only recently, the lift-off characteristics of biodiesel fuel (soy methyl ester) were investigated by Lee and co-workers[21] and Mueller et al.[22] Lee and co-workers[21] measured flame lift-off in a constant volume combustion vessel with optical access ports and observed that lift-off length of biodiesel was higher than that of diesel 2 fuel. They also observed significant reduction of soot for biodiesel fuel. Mueller et al.[22] measured flame lift-off lengths in a single-cylinder engine with optical access and observed that lift-off length of a diesel-like fuel (with a CN of 45) was marginally higher than that of biodiesel.

Previous studies by Som et al.[23] have identified the differences in inner-nozzle flow, as well as non-evaporating and evaporating spray characteristics of diesel and biodiesel fuels using computational tools. The current work extends previous studies under non-reacting conditions by including detailed kinetic models for the oxidation of these fuels along with emission models for soot and $NO_x$ formation. The major objective of the present study is to quantify differences between the combustion and emission characteristics of diesel and biodiesel fuels. Because there are significant differences in the thermo-transport and chemical properties of these fuels, the combustion and emission characteristics of biodiesel can be expected to differ from those of diesel. Detailed two-phase-flow simulations were performed in an engine modeling software, CONVERGE,[24−26] to examine the combustion and emission characteristics of diesel and biodiesel fuels under diesel engine conditions.

The difference in $NO_x$ emission characteristics of diesel and biodiesel has recently been investigated.[22,27] Mueller et al.[22] summarized different reasons for the $NO_x$ increase with biodiesel under various engine conditions. The reasons include fluid dynamics effects, such as higher residence time inside the combustion chamber for biodiesel, chemical kinetic pathways, such as an increase in prompt $NO_x$ because of higher concentrations of CH for biodiesel fuel, and the radiative heat-transfer effect. The oxidation chemistry of various surrogates used in CI engines to model diesel and biodiesel fuels may also influence the $NO_x$ emission characteristics. This aspect is further analyzed in this study. Also, to isolate the influence of fluid dynamics and radiative heat transfer from chemical kinetics of $NO_x$ formation, ignition and flame simulations were performed in CHEMKIN software,[28] which is an industry standard tool for studying the gas-phase chemical kinetic behavior of different fuels.

**Table 1. Comparison of Nozzle Exit Conditions for Diesel and Soy Biodiesel**

| property | diesel | biodiesel |
|---|---|---|
| total mass injected (mg) | 17.706 | 15.940 |
| discharge coefficient ($C_d$) | 0.64 | 0.62 |
| area coefficient ($C_a$) | 0.91\|0.91 | 1\|1 |
| turbulent kinetic energy (TKE) ($m^2/s^2$) | 2500 | 2200 |
| turbulent dissipation rate (TDR) ($m^2/s^3$) | $4.23 \times 10^9$ | $3.24 \times 10^9$ |

## 2. COMPUTATIONAL PHYSICAL MODEL

**2.1. Zero-Dimensional (0D) and One-Dimensional (1D) Combustion Simulations.** The simulations in simplified combustion systems, such as 0D and 1D reactors, are performed in CHEMKIN software.[28] Gas-phase autoignition delay at different equivalence ratios, ambient pressures, and ambient temperatures for diesel and biodiesel fuel surrogates are calculated using the perfectly stirred reactor (PSR) application. Laminar burning velocities of these surrogates are predicted using the PREMIX application.[29] Diffusion flame simulations are performed using the OPPDIF application.[30] The grid independence of the 1D results was achieved using adaptive regridding to resolve the structure of the reaction zone.

**2.2. Three-Dimensional (3D) Combustion Simulations.** Fuel spray and combustion simulations were performed using the Eulerian−Lagrangian approach in the computational fluid dynamics (CFD) software CONVERGE.[24−26] It incorporates state-of-the-art models for spray injection, atomization and breakup, turbulence, droplet collision, and coalescence. The gas-phase flow field is described using the Favre-averaged Navier−Stokes equations in conjunction with the renormalization group theory (RNG) $k-\varepsilon$ turbulence model, which includes source terms for the effects of the dispersed phase on gas-phase turbulence. These equations are solved using a finite volume solver. The details of these models can be found in previous publications;[19,25,26,32] therefore, only a brief description is provided here.

In our previous studies,[23] significant differences between the injector flow characteristics of biodiesel and diesel fuels were observed. A cylindrical nozzle orifice with an orifice diameter of 169 $\mu$m and length/diameter ratio of 4.2 was employed. In particular, the cavitation (represented by area coefficient, $C_a$) and turbulence levels were lower for biodiesel compared to those for diesel, and this was attributed to the lower vapor pressure and higher viscosity of biodiesel. In addition, the injection velocity, discharge coefficient, and mass flow rate predicted by simulations were lower for biodiesel (cf. Table 1), because of its higher viscosity. This is consistent with experimental observations by Miers et al.[31] A coupling approach was developed to account for the influence of inner-nozzle flow effects on spray and combustion simulations. After injection, the liquid breakup was simulated using primary Kelvin−Helmholtz−aerodynamics cavitation turbulence (KH−ACT) and secondary Kelvin−Helmholtz−Rayleigh−Taylor (KH-RT) breakup models. Details of the KH−ACT primary breakup model and coupling developed and validated by our group are provided in refs 32−34. The KH−ACT model captures the effects of cavitation and turbulence on primary breakup, in addition to aerodynamic breakup. Biodiesel exhibited poor atomization characteristics compared to diesel; the spray penetration and Sauter mean diameter (SMD) were higher, while dispersion and cone angle were smaller for biodiesel, consistent with experimental trends reported in the literature. These experimental trends could not be accurately captured by the Kelvin−Helmholtz (KH) primary breakup model, but they were captured by the KH−ACT

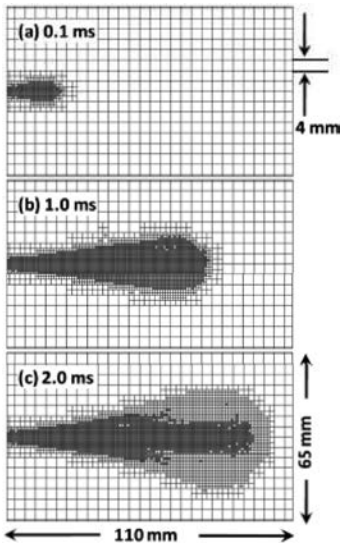


**Figure 1.** Grid generated in CONVERGE at different times during the simulation for combusting sprays described in Table 2. The field of view in axial and radial direction is about 110 and 65 mm, respectively.

model, thus demonstrating the effectiveness of the latter in predicting the primary breakup phenomenon.

The KH and Rayleigh−Taylor (RT) models are used to predict the subsequent secondary droplet breakup.[35,36] Droplet collisions are based on the no time counter (NTC) algorithm.[37] Once collision occurs, the outcomes of the collision are predicted as bouncing, stretching, reflexively separating, or coalescing.[38] A droplet evaporation model based on the Frossling correlation is used.[32] A dynamic drag model is used that postulates that the drag coefficient depends upon the shape of the droplet, which can vary between a sphere and a disk. An initially spherical droplet distorts significantly when the Weber number is large. The drag coefficient for a disk is significantly higher than that for a sphere. This dynamic drag model accounts for the effects of drop distortion, varying linearly between the drag of a sphere and a disk.[39] The effects of turbulence on the droplet are also included, using a turbulent dispersion model.

Detailed kinetic modeling is performed using the SAGE chemical kinetic solver[24,26] and is directly coupled with the gas-phase calculations using a well-stirred reactor model. NHPT is used as a surrogate for diesel fuel, while a mixture of MB and NHPT is used as a surrogate for soy biodiesel fuel. The NHPT mechanism was developed at Chalmers University[40] and consists of 42 species and 168 reactions. The reduced mechanism for biodiesel combustion[11] is comprised of 33% MB and 67% NHPT and consists of 41 species and 150 reactions. To examine the $NO_x$ emission characteristics, a reduced $NO_x$ model[41] from the GRI-3.0 mechanism[42] was incorporated into the NHPT and biodiesel mechanisms. This $NO_x$ chemistry model has been previously validated against flame measurements at different conditions.[43] A few hundred elementary-gas-phase reactions are involved in the formation of $NO_x$, which can be formed or destroyed by at least five separate reaction processes.[44] They are classified as thermal, prompt, $N_2O$, NNH, and reburn routes. Under CI engine conditions, the $NO_x$ formation mainly occurs through thermal, prompt, and $N_2O$ routes,[45] which are investigated further. The soot mass production within a computation cell is determined from a single-step competition between formation and oxidation rates of $C_2H_2$ species based on the Hiroyasu model.[26,32] This soot model has been extensively used in engine-modeling literature.[19,24,32,49]

CONVERGE uses an innovative, modified cut-cell Cartesian method for grid generation. The grid is generated internally to the code at runtime. For all cases, the base grid size was fixed at 4 mm. To resolve the flow near the injector, a fixed grid embedding is employed such that the minimum grid size is 0.5 mm based on a previous study.[46] As discussed in the cited and many other studies, spray simulations using a Euler-ain−Lagrangian approach are not grid-independent because of the fundamental assumption of the liquid volume fraction being much smaller than the cell volume. Reducing the grid size below a certain value (0.4 mm in the present study) makes this assumption questionable and may also lead to convergence difficulties. The spray penetration is overpredicted on a coarse grid and underpredicted on a fine grid.[47] Hence, an optimum grid size was identified, which resulted in a reasonable computational time and yielded good agreement with measurements. Moreover, this is a standard approach employed for engine combustion simulations.[48,49] Apart from this region, it is rather difficult to determine *a priori* where a refined grid is needed. Hence, three levels of adaptive mesh refinement are employed for the velocity field, such that the minimum grid size is 0.5 mm. To match the combustion chamber geometry used in the experimental study,[21] a cylindrical geometry of 65 mm in diameter and 110 mm in length is generated (cf. Figure 1). The temperature-dependent fuel properties of diesel and soy biodiesel, such as density, kinematic viscosity, surface tension, vapor pressure, heat of vaporization, and specific heat, were obtained from Ra et al.[12]

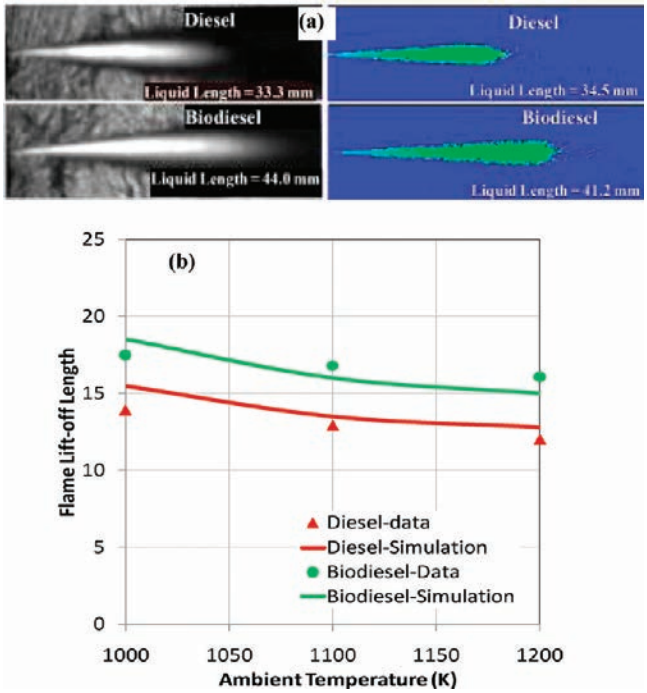


**Figure 2.** (a) Measured[45] and predicted spray structures for diesel and biodiesel at an ambient temperature of 1000 K. (b) Measured[20] and predicted flame lift-off lengths versus ambient temperature for diesel and biodiesel fuels.

## 3. RESULTS AND DISCUSSION

**3.1. Validation.** Extensive validations of 3D evaporating and combusting spray simulations for diesel fuel have been reported in our previous studies.[19,32] Soot model validation against planar laser-induced incandescence (PLII) data from Sandia National Laboratory has also been performed.[32] The current validation effort focuses on liquid and lift-off length validation for biodiesel fuel. Figure 2a presents a comparison of the measured[50] and predicted spray structures for diesel and soy biodiesel at an ambient temperature of 1000 K, ambient density of 14.8 kg/m$^3$, orifice

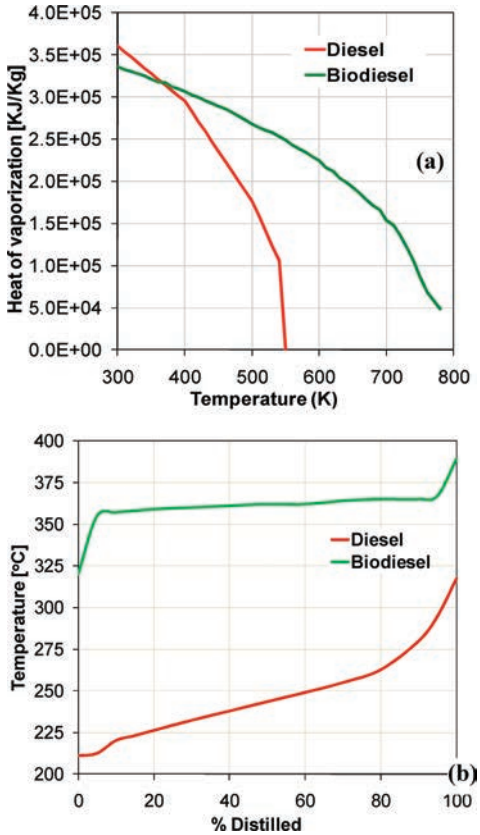


**Figure 3.** (a) Heat of vaporization versus temperature. (b) Distillation curves for diesel (diesel fuel 2) and soy biodiesel fuels.

diameter of 246 $\mu$m, injection pressure of 142 MPa, and an injection duration of 5 ms. The measured spray structure is presented in terms of the superimposed Mie and Schlieren images, while the predicted structure is in terms of the droplet parcel locations during the quasi-steady period [i.e., at 2.0 ms from start of injection (SOI)]. The field of view in the axial and radial directions is 50 and 15 mm, respectively. The maximum liquid phase fuel penetration (defined by an axial position that encompasses 97% of the injected fuel mass at a given time instant from the start of injection) is called the liquid length. Liquid penetration is an important parameter for diesel combustion because overpenetration can result in spray wall impingement, while underpenetration can result in underutilization of ambient air. The predictions reproduce the experimental trend in terms of the higher liquid penetration for biodiesel compared to diesel. Higher liquid length for biodiesel compared to that of diesel can be mainly attributed to two reasons: (1) The distillation curve and heat of vaporization of biodiesel is higher, as shown in Figure 3. Biodiesel vaporizes at higher temperatures; thus, more energy needs to be supplied. This results in higher volatility with biodiesel and, hence, higher liquid penetration lengths. This is the main reason because spray vaporization is mixing-controlled under CI engine conditions. (2) There is a reduced breakup because of a lower amount of cavitation and turbulence at the nozzle exit. Lesser breakup results in larger droplets carrying greater momentum and, thus, penetrating further. If spray breakup characteristics were more important, the differences in non-evaporating spray penetration characteristics between diesel and biodiesel would be larger. This is not the case, as seen from our previous publications.[23]

**Table 2. Range of Conditions for Combusting Spray Experiments Performed by Wu et al.[22]**

| parameter | quantity |
|---|---|
| injection system | common rail |
| number of orifices | 6 |
| nozzle type | valve-covered orifice (VCO) |
| orifice diameter ($\mu$m) | 145 |
| injection pressure (bar) | 1340 |
| injection quantity (mm$^3$) | 20 per orifice |
| chamber density (kg/m$^3$) | 15 |
| chamber temperature (K) | 1000−1200<br>base case: $T$ = 1000 K |
| ambient $O_2$ concentration (%) | 21 |
| fuel temperature (K) | 353 |
| injection duration (ms) | 3.5 |

Figure 2b presents a comparison of the measured[21] and predicted flame lift-off lengths for diesel and biodiesel fuels at different ambient temperature conditions, tabulated in Table 2. In simulations, the flame lift-off length is determined by the farthest upstream location of the 2200 K temperature contour from the point of injection (POI). This is relatively easy to calculate because temperature gradients are strong near the flame surface. Thus, liquid length is a global parameter for the atomization and vaporization behavior, whereas the lift-off length is used to represent the combustion behavior. An increase in the ambient temperature (keeping ambient density constant) results in lowering of the flame lift-off length because of an increase in flame reactivity, which moves the ignition and flame stabilization locations upstream. The measured lift-off length is marginally higher for biodiesel compared to diesel. Simulations are able to capture the flame lift-off characteristics of these fuels very well. It is interesting to note that the simulations underpredict lift-off length for biodiesel and overpredict lift-off length for diesel fuel, especially at higher ambient temperatures. However, these differences between experiments and simulations are well within the uncertainty of the measurements. Hence, further analysis is performed to gain insight about the ignition and flame stabilization characteristics of biodiesel compared to that of diesel.

**3.2. Ignition and Flame Stabilization Characteristics.** Figure 4a presents liquid and lift-off lengths for diesel and biodiesel versus time from SOI for the simulated cases described in the context of Figure 2b and tabulated in Table 2, at an ambient temperature of 1000 K. Liquid penetration is seen to increase to a certain value and then stabilize at about 0.5 ms from SOI. The liquid length is established at a location where the fuel-injection rate balances the fuel-evaporation rate.[51] The fluctuations in the liquid length of both fuels are turbulence-induced. The liquid length for biodiesel is about 8−9 mm higher than that of diesel under the conditions investigated, which is consistent with results reported earlier in this study (cf. Figure 2a). The flame is established upstream of the liquid length, then is seen to move downstream toward the injector for both the fuels, and stabilizes at about 1.75 ms from SOI. It is interesting to note that, for diesel fuel (under the conditions investigated), lift-off length is always higher than liquid length. However, for biodiesel fuel, lift-off length is lower than liquid length after 0.75 ms from SOI. As mentioned earlier, the interplay between liquid length and lift-off length has important implications for in-cylinder compression

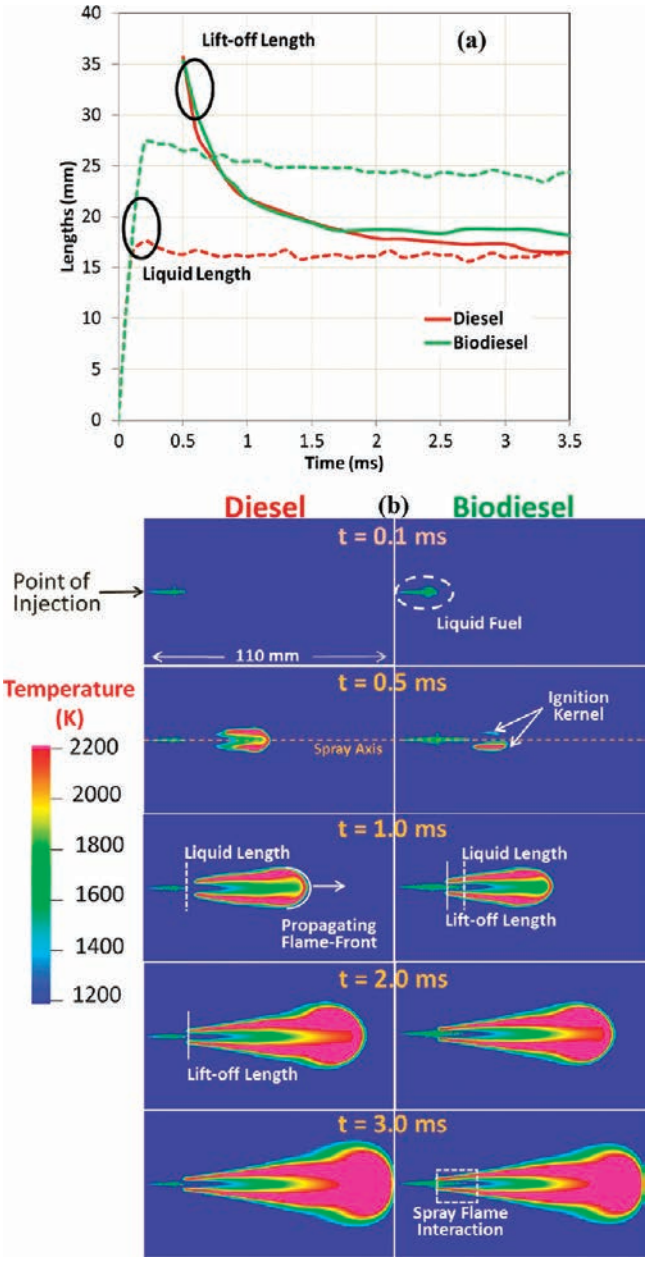


**Figure 4.** (a) Liquid length and flame lift-off length versus time from SOI. (b) Computed liquid fuel penetration and temperature contours, for diesel and biodiesel fuels corresponding to the base case.

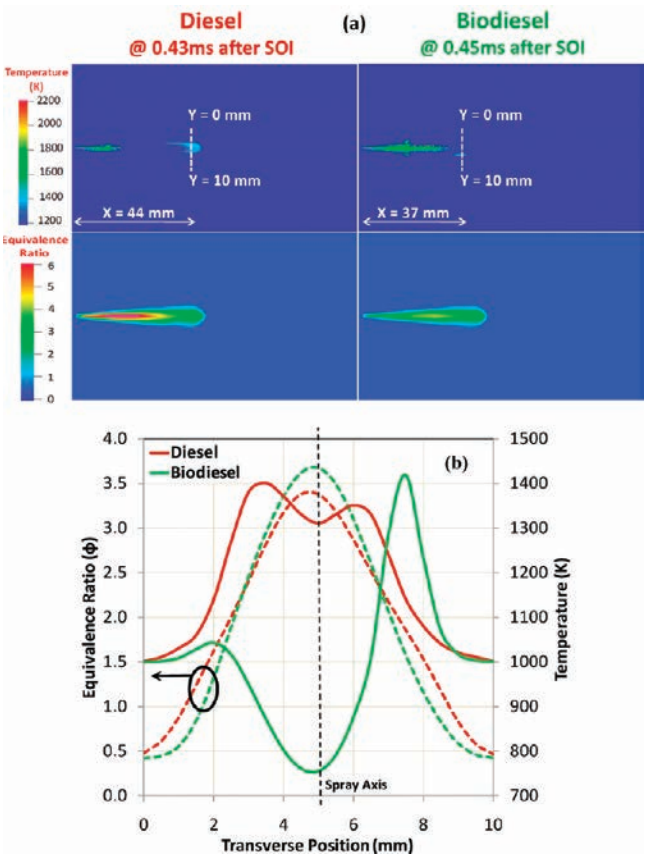


**Figure 5.** (a) Temperature and equivalence ratio contours for diesel and biodiesel when ignition occurs. Axial ignition location and liquid fuel spray (green droplets) are also shown. (b) Temperature and equivalence ratio distribution versus transverse position (demarcated in Figure 5a) at the axial location of ignition and time for diesel and biodiesel fuels. The spray axis is also shown.

engine processes. Clearly, for biodiesel, there is more interaction between the spray and combustion processes, which is also seen in the context of Figure 4b.

The corresponding computed flame images (including liquid and lift-off locations) at representative times are shown in Figure 4b. The field of view is 110 × 65 mm in the axial and radial directions, respectively. The direction and POI are also marked. Because of the axisymmetric nature of the spray and combustion processes, images are presented on a cut plane through the center of the fuel jet. Liquid fuel is shown with green color droplets at 0.1 ms from SOI for both fuels. While the penetration is similar for both the fuels, clearly, the spray is broader for biodiesel, mainly because of its higher heat of vaporization. The occurrence of ignition is indicated by the appearance of two flame kernels downstream of the liquid fuel at 0.5 ms after SOI. The flame is asymmetrical about the spray axis and is more developed for diesel fuel. The asymmetry is attributed to an insufficient number of spray parcels residing in the domain, especially at 0.5 ms after SOI. This is mainly due to enhanced breakup, owing to a higher amount of inner nozzle cavitation and turbulence (cf. Table 1) for diesel fuel. The difference in the ignition delay of both fuels is further investigated in detail in the following text.

As the flame front develops and propagates downstream, the ignition location (base of the flame) seemingly moves upstream, as indicated in $t$ = 1.0 and 2.0 ms plots. The flame base is stabilized at about 1.5 ms after SOI at the lift-off length, which is marked by the white solid line. The established liquid length for both of the fuels is also shown at 1 ms, marked by white dashed lines. After 3 ms from SOI, the flame front is seen to reach the end wall of the combustion chamber. More importantly, the spray flame interaction shown by the liquid fuel droplets entering the high-temperature combustion regions, i.e., the lift-off length being shorter than the liquid length, is clearly seen. This aspect is also further analyzed at higher ambient temperature conditions in the next section.

In Figure 5, the ignition characteristics of diesel and biodiesel are studied further. Figure 5a plots the temperature (top) and equivalence ratio (bottom) contours at the instant ignition occurs

**Table 3. Comparison of Physical Properties of Diesel and Soy Biodiesel Used in the Simulations**

| fuel property | diesel | biodiesel |
|---|---|---|
| carbon content (wt %) | 87 | 76.74 |
| hydrogen content (wt %) | 13 | 12.01 |
| oxygen content (wt %) | 0 | 11.25 |
| density at 15 °C (kg/m$^3$) | 820 | 885.3 |
| dynamic viscosity at 40 °C (cP) | 1.69 | 5.626 |
| surface tension at 25 °C (N/m) | 0.0020 | 0.00296 |
| vapor pressure at 25 °C (Pa) | 1000 | 1 |

for these fuels. The field of view is 110 × 65 mm in the axial and radial directions, respectively. The axial location of ignition is marked by a dashed white line. Ignition is characterized by cell temperatures greater than 1400 K and is seen to occur closer to the nozzle orifice for biodiesel (i.e., at 37 mm) compared to diesel (44 mm), which is mainly attributed to the oxygen content in biodiesel fuel (cf. Table 3). Higher fuel spray penetration for biodiesel is also observed in the temperature contours plots, which has been discussed in detail earlier. The equivalence ratio plot shows lower values for biodiesel fuel, especially in the spray-core region. This is mainly due to two reasons: (1) The amount of biodiesel injected is about 10% less than that of diesel. (2) There is less amount of fuel evaporation for biodiesel because of its higher heat of vaporization and distillation curves (cf. Figure 3). Because the equivalence ratio is calculated on the basis of gas-phase mole fractions, smaller equivalence ratio values for biodiesel are not surprising. It should be noted that the temperature of the spray core increases because of entrainment of hot ambient air. However, the temperature in the core is not high enough for complete evaporation of these fuels. Under compression engine conditions, wherein the expansion stroke is modeled, almost 99% of the injected fuel evaporates. However, in the current simulations, the injection duration is set equal to the simulation time; hence, all of the injected fuel does not evaporate. This fact is observed in Figure 4b for both of the fuels because, even at 3 ms from SOI (nearing end of injection at 3.5 ms), a significant amount of fuel (green droplets) is observed near the spray core for both of the fuels.

Figure 5b plots the temperature and equivalence ratio versus transverse position at the instant and location of ignition, i.e., at 0.43 ms from SOI and 44 mm from POI for diesel and 0.45 ms from SOI and 37 mm from POI for biodiesel. The temperature in the spray core is lower for biodiesel, which also shows lower amounts of ambient air entrainment. This can be directly correlated to the fact that lesser spray atomization and breakup has been observed for biodiesel by Som et al.[23] Enhanced breakup ensures smaller droplets, which spread more, and increases air entrainment, which is the case with diesel fuel. Ignition locations are marked by dashed lines for both of the fuels. Ignition is seen to occur in rich mixtures for both of the fuels. The equivalence ratio range for ignition is $2.5 \leq \Phi \leq 3.0$ and $1.4 \leq \Phi \leq 1.8$ for diesel and biodiesel, respectively. The corresponding oxygen equivalence ratio range ($\Phi_\Omega$) for biodiesel[52] is $1.33 \leq \Phi_\Omega \leq 1.63$. This highlights the need for ignition delay data at richer mixture conditions rather than at stoichiometric ($\Phi = 1$) values. Under CI engine conditions, the diffusion flame is established at stoichiometric values and may not be due to an autoignition mechanism. It should also be noted that fuel-rich ($\Phi > 1$) chemical kinetics of combustion is different from stoichiometric and fuel-lean ($\Phi < 1$) kinetics.

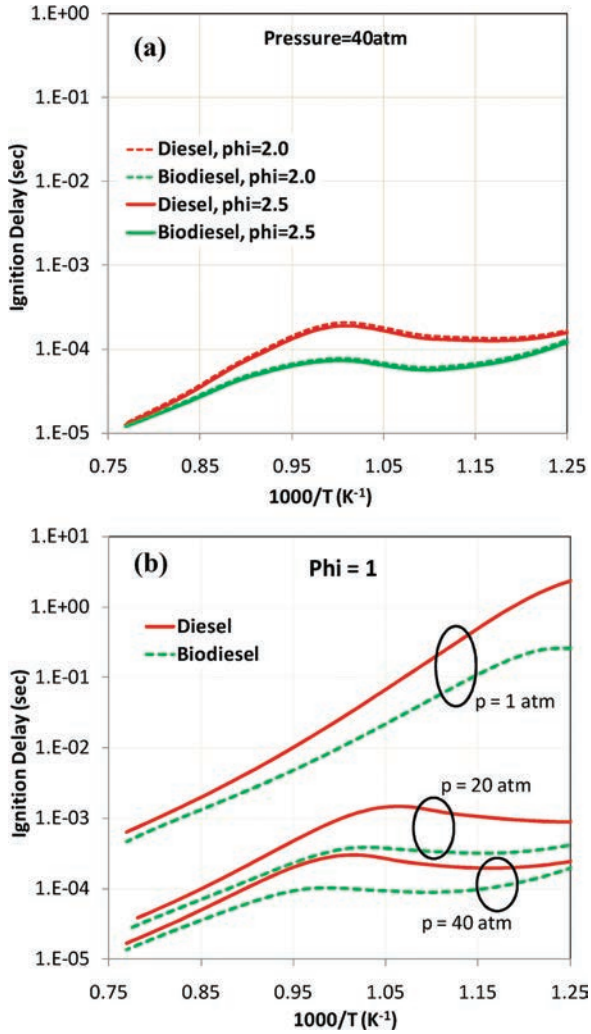


**Figure 6.** Ignition delay times as a function of the ambient temperature for diesel and biodiesel fuels (a) at different equivalence ratios (rich conditions) and ambient pressure of 40 atm and (b) at different ambient pressures for stoichiometric mixtures.

The ignition delay times reported in Figure 5a are 0.43 and 0.45 ms for diesel and biodiesel, respectively. These delay times account for both physical and chemical ignition delay. The physical delay is influenced by (1) ambient conditions, such as density, temperature, velocity, and turbulence, (2) fuel properties, such as density, viscosity, surface tension, specific heat, heat of vaporization, etc., which in turn influences (3) the near nozzle atomization and penetration characteristics, along with the spray shape. Once an autoignitable fuel−air mixture is formed, for ignition to occur, radicals are necessary, which can happen once the chemical bonds are broken. Biodiesel has a higher CN and is typically between 46 and 52 and 56 and 60[1] for vegetable-oil- and animal-fat-based feedstocks, respectively. The CN for diesel fuel in North America is typically in the range of 40−45,[1] which usually results in higher ignition delay times compared to biodiesel. However, the simulations predict that ignition delay times are higher for the biodiesel surrogate. It is expected that the physical delay is higher for biodiesel because of the slower breakup and larger SMD values.[23]

The chemical ignition delay characteristics of diesel and biodiesel surrogates are further investigated in Figure 6, which

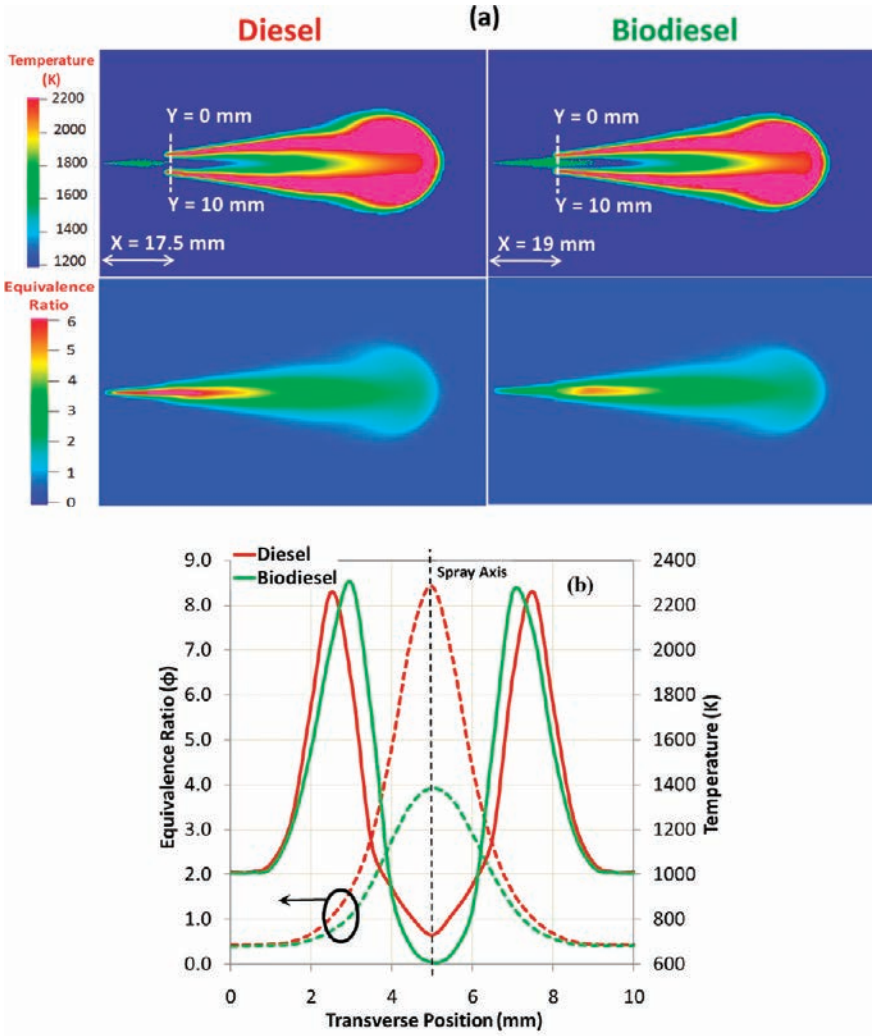


**Figure 7.** (a) Temperature and equivalence ratio contours for diesel and biodiesel fuels at 2 ms from SOI. Flame lift-off length and liquid fuel spray (green droplets) are also shown. (b) Temperature and equivalence ratio distribution versus transverse position (demarcated in Figure 7a) at flame lift-off location and 2 ms from SOI, for diesel and biodiesel fuels. The spray axis is also shown.

plots the delay times as a function of the ambient temperature at different equivalence ratios and ambient pressure conditions. These simulations were performed using the PSR package in CHEMKIN software. It is assumed that ignition occurs when $T \geq 1400$ K. Under all of the conditions investigated, chemical ignition delay times were higher for the diesel surrogate compared to biodiesel. In addition, an increase in the equivalence ratio or ambient pressure results in lower chemical ignition delay times, which is consistent with results reported in the literature.[8] While the chemical ignition delay times for the fuel surrogates predict accurate delay trends, the fact that the expected overall ignition delay times are not predicted by the fuel surrogates warrants further investigation. The CN for NHPT and MB + NHPT mixtures are approximately 53 and 33, respectively. This suggests that improved fuel surrogate mechanisms need to be developed to ensure that the CN of surrogate mixtures are closer to the fuel of interest. In our recent study,[53] the focus was toward development of a methyl-decanoate-, methyl-decenoate-, and NHPT-based chemical kinetic model for high-temperature flame applications. Low-temperature combustion chemistry will be added to this mechanism in the future, to perform CI engine simulations. Because the CN for methyl decanoate is about 47, it is expected to be more representative for biodiesel combustion and ignition.

Figure 7a plots the temperature (top) and equivalence ratio (bottom) contours at 2 ms from SOI for these fuels. The field of view is 110 × 65 mm in the axial and radial directions, respectively. The flame lift-off lengths are 17.5 and 19 mm, respectively, for diesel and biodiesel. For both of the fuels, the spray and flame seem to be fairly symmetrical around the spray axis. The equivalence ratio plot again shows higher values for diesel fuel in the spray core region, the reasons for which have been explained in the context of Figure 7. In our recent study,[23] the vapor penetration was plotted by showing the equivalence ratio contours at different times from SOI for diesel and biodiesel fuels. It was observed that, after 0.5 ms from SOI, vapor penetration was higher for biodiesel compared to diesel under evaporating but non-combusting conditions. Such differences in vapor penetration are not seen here under combusting conditions because the vapor downstream of the liquid spray region participates in combustion. Nevertheless, vapor penetration is still marginally higher for biodiesel.

Figure 7b plots the temperature and equivalence ratio versus transverse position at the flame lift-off location for diesel (17.5 mm)

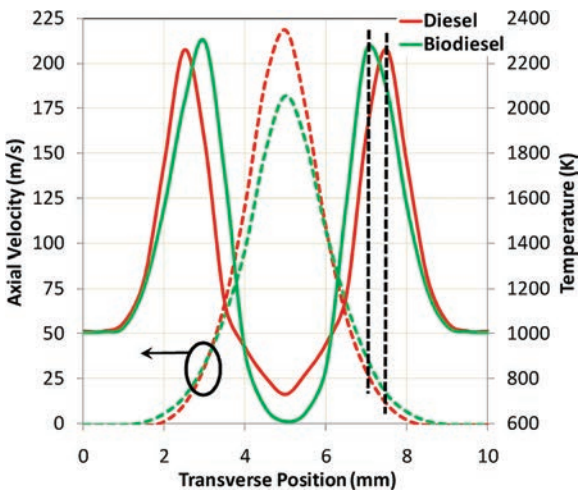


**Figure 8.** Gas-phase axial velocity and temperature distribution versus transverse position (demarcated in Figure 7a) at the flame lift-off location and 2 ms from SOI, for diesel and biodiesel fuels. Black dashed lines show transverse location of flame stabilization.

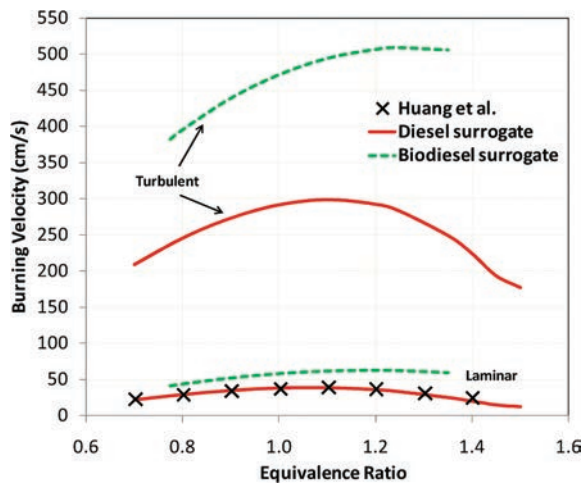


**Figure 9.** Laminar and turbulent burning velocity versus equivalence ratio for diesel and biodiesel surrogates. Data from Huang et al.[50] for NHPT−air mixture flame speeds is also shown.

and biodiesel (19 mm), discussed in the context of Figure 7a. The temperature peaks are closer to the spray axis for biodiesel because of two reasons: (1) The stoichiometric surface for biodiesel occurs at a higher value of the mixture fraction compared to diesel fuel[54] because of differences in the stoichiometric fuel−air equivalence ratio (∼1:14.5 and ∼1:12.5 for diesel and biodiesel, respectively). This implies that the flame surface and, hence, the temperature peaks are closer to the spray axis for biodiesel compared to diesel fuel. (2) There is a reduced spray breakup for biodiesel. As seen earlier (cf. Figure 5b), the temperature in the spray core is lower for biodiesel because of a lesser amount of ambient air entrainment. However, the equivalence ratios are significantly lower for biodiesel, especially near the spray core, which is again due to a lesser amount of fuel evaporation. At the lift-off location ($T \geq 2200$ K), the equivalence ratios are close to stoichiometric for both of the fuels, representing a diffusion flame. Naber and Siebers[55] derived the following correlation to calculate the equivalence ratio at the flame lift-off location for diesel fuel:[17,18]

$$\phi(X) = \frac{30}{\left[\sqrt{1+16X^2}-1\right]} \tag{1}$$

where

$$X = \frac{L_f}{X^+} \tag{2}$$

$$X^+ = \sqrt{\frac{\rho_f}{\rho_a}}\left(\frac{\sqrt{C_a}d}{0.66\tan(\theta/2)}\right) \tag{3}$$

where $L_f$ is the flame lift-off length, $\rho_f$ and $\rho_a$ are fuel and ambient densities, respectively, $C_a = 0.91$, $\theta = 12.5°$, and $d$ (nozzle diameter) = 145 $\mu$m. From eqs 1 to 3, the equivalence ratio at the axial location of flame lift-off is found to be about 6.4. From simulations, the average equivalence ratio in the spray core (where $T \leq 1000$ K) at the axial position of flame lift-off is found to be about 6.3, which is in good agreement with the correlations.

Figures 8 and 9 investigate the flame stabilization characteristics for diesel and biodiesel fuels. Figure 8 plots the corresponding gas-phase axial velocity and temperature distribution at the flame lift-off location for diesel (17.5 mm from POI) and biodiesel (19 mm from POI) versus the transverse position described in the context of Figure 7a. In the center of the flame, the gas-phase axial velocities are higher for diesel, which is due to the fact that the liquid phase injection velocities were also higher.[23] The transverse flame stabilization location is shown by dashed black lines. The axial velocity at the flame stabilization location seems to be lower for diesel compared to biodiesel. This aspect is further investigated in the next paragraph.

Figure 9 plots the laminar and turbulent burning velocities for both of the fuels. The laminar burning velocities were calculated using the PREMIX application in CHEMKIN software for different mixture compositions. For both of the fuels, the reference temperature ($T_{u,ref}$) and pressure ($P_{ref}$) conditions were chosen to be 300 K and 1 bar. Experimental burning velocity data under these conditions was available from Huang et al.,[56] for NHPT only. As mentioned earlier, NHPT is used as a diesel surrogate, while a mixture of MB and NHPT is used as a biodiesel surrogate. There is excellent agreement between the simulations and experiments in terms of laminar burning velocities ($S_{L,ref}$) for NHPT at the reference condition. Although difficult to observe here, the laminar burning velocities are about 1.5 times higher for the biodiesel surrogate. The peak burning velocity was at $\Phi = 1.05$ for diesel surrogate and $\Phi = 1.2$ for the biodiesel surrogate. The laminar burning velocity ($S_L$) at different temperature ($T_u = 1000$ K) and pressure ($P_u = 40$ bar) conditions can be estimated on the basis of the correlation by Turns[57]

$$S_L = S_{L,\,ref}\left(\frac{T_u}{T_{u,\,ref}}\right)^{\gamma}\left(\frac{P_u}{P_{ref}}\right)^{\beta}(1-2.1Y_{dil}) \tag{4}$$

where $Y_{dil}$ is the extent of dilution, which in this case is 0.

$$\begin{aligned}\gamma &= 2.18 - 0.8(\phi - 1)\\ \beta &= -0.16 + 0.22(\phi - 1)\end{aligned} \tag{5}$$

where $\Phi$ is the equivalence ratio. The turbulent flame speed can then be approximated on the basis of the following correlation:[57]

$$S_T = S_L\left(0.5\left[1 + \left(1 + 8\left(\frac{u'}{S_L}\right)^2\right)^{0.5}\right]\right)^{0.5} \quad (6)$$

where $u'$ is the turbulent velocity fluctuation calculated from the turbulent kinetic energy ($k$) as follows:

$$u' = \sqrt{\frac{2}{3}k} \quad (7)$$

The turbulent kinetic energy values at the flame lift-off location were available from the 3D combustion simulations.

The turbulent burning velocities calculated from eqs 4 to 7 are also plotted in Figure 9. The turbulent burning velocities are orders of magnitude higher than the laminar values, which is expected. The turbulent burning velocity for the biodiesel surrogate is about 2 times greater than that of the diesel surrogate at all equivalence ratios. This is due to the fact that the turbulence kinetic energy is also higher for biodiesel. According to Peters,[58] the flame lift-off location (under turbulent conditions with gas-jet injection) is determined by a balance between the turbulent burning velocity and local flow velocity. Hence, it is not surprising that the turbulent lifted flame is stabilized at higher gas-phase velocity values for biodiesel compared to diesel. Because the turbulent burning velocity for both of the fuels is significantly lower than the gas-phase axial velocities, it is unlikely that the mechanism of flame stabilization is propagation-based. Under the conditions investigated, there is no evidence of ignition kernels upstream and detached from high-temperature reaction zones for both fuels, as was observed by Pickett et al.[59] In fact, flame stabilization seems to occur because of successive autoignition of incoming fuel at the flame lift-off location[49] for both of the fuels. It should also be noted that these simulations were Reynolds-averaged Navier–Stokes (RANS)-based, where the average concentration of species and temperature may be too low for autoignition. Large eddy simulation (LES) methods, which are more accurate than RANS methods, can capture the instantaneous species and temperature profiles, which can lead to more autoignition zones. However, LES methods are computationally more expensive; hence, they will be employed in future studies.

**3.3. Parametric Studies.** Extensive validation of liquid and lift-off length characteristics of diesel fuel have been performed in our previous studies.[19,32] However, because of the lack of experimental data, such validation studies are not feasible for biodiesel. Because the flame lift-off characteristics under different ambient temperature conditions were well-predicted in simulations (cf. Figure 2b), parametric studies were performed to characterize the influence of other parameters, such as ambient gas density, temperature, and oxygen concentration, on liquid and lift-off lengths for biodiesel. Figure 10a presents the influence of the ambient temperature (at a fixed ambient density of 15 kg/m$^3$ and $O_2$ concentration of 21%), on liquid and lift-off lengths for both of the fuels. Both liquid and lift-off lengths are higher for biodiesel at all temperatures. It is interesting to note that the crossover temperature (i.e., the temperature beyond which the liquid length is higher than the flame lift-off length) is about 975 and 850 K for diesel and biodiesel, respectively. This shows more interplay between the spray and combustion processes for biodiesel fuel.

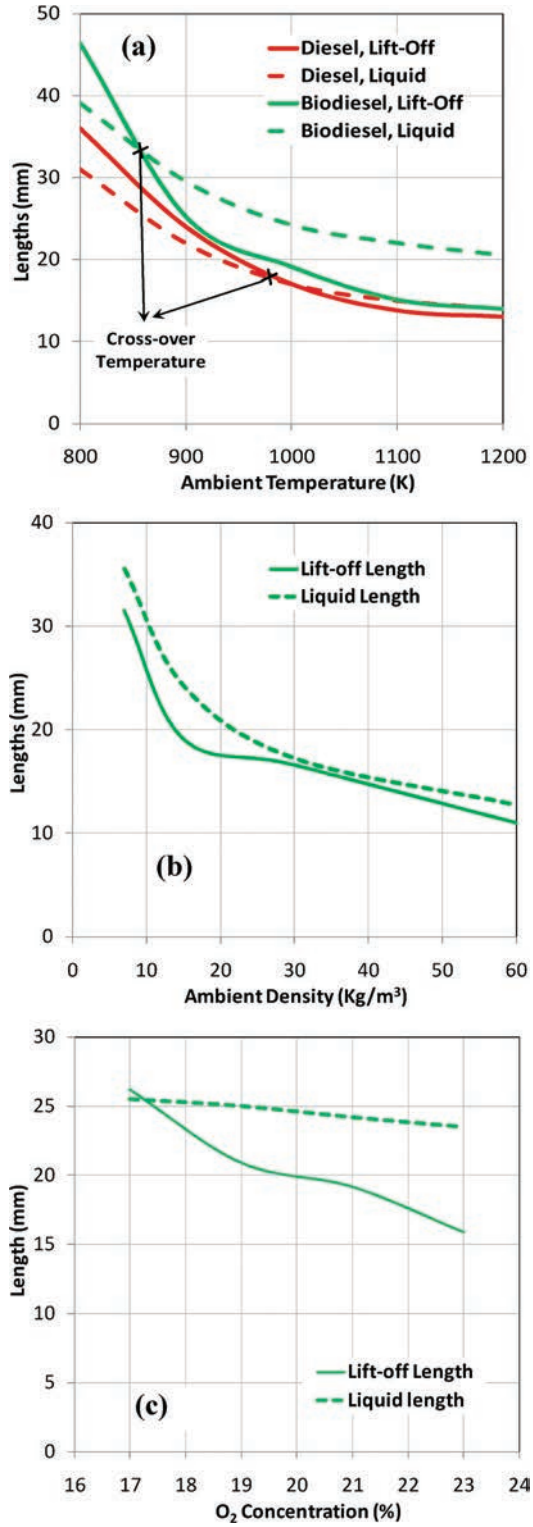


**Figure 10.** Influence of the (a) ambient temperature, (b) ambient density, and (c) ambient oxygen concentration on liquid and flame lift-off lengths for biodiesel fuel. A comparison of crossover temperatures between diesel and biodiesel fuels is also shown in panel a.

As the ambient density (or ambient pressure) increases (at a fixed ambient temperature of 1000 K and $O_2$ concentration of 21%), it decreases the injection velocity at the nozzle exit and, consequently, decreases the liquid length (cf. Figure 10b). The

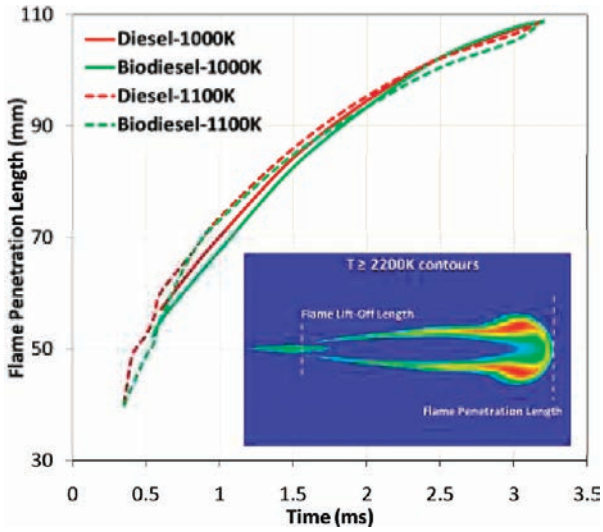


**Figure 11.** Flame penetration length versus time from SOI for both diesel and biodiesel fuels. The inset plots temperature contours ($T \geq$ 2200 K) demarcating the flame lift-off position and flame length. The liquid fuel spray is shown by green droplets.

liquid length also decreases because of the increased droplet drag caused by higher ambient density. Under the ambient density conditions investigated, for biodiesel, the liquid length is always higher than the lift-off length. Figure 10c shows the effect of the ambient oxygen concentration (at a fixed ambient temperature of 1000 K and ambient density of 15 kg/m$^3$) on the flame structure and stabilization location. As the oxygen concentration is reduced, it decreases the flame reactivity (or the Damköhler number) and effectively enhances the EGR effect. As a consequence, the ignition location and the flame base move downstream, increasing the flame lift-off length. Another reason for the flame location to move downstream with a decreasing oxygen concentration is because more air entrainment is necessary to form autoignitable fuel−air mixtures.

In the previous section, the ignition and flame lift-off characteristics of diesel and biodiesel were investigated in detail. In this section, parametric studies are performed to investigate the influence of the ambient temperature ($T$ = 1100 K) for a fixed ambient density of 15 kg/m$^3$ on the flame stabilization mechanism for diesel and biodiesel under conditions tabulated in Table 2. Figure 11 plots flame penetration lengths for diesel and biodiesel at two different temperatures of 1000 and 1100 K. In simulations, while the flame lift-off length is defined as the farthest upstream location of $T \geq$ 2200 K contour, the flame penetration length is defined by the farthest downstream location of $T \geq$ 2200 K contour. A higher flame penetration length results in flame quenching or extinction at the cooler walls of the combustion chamber, which act as a heat sink. While the flame lift-off characteristics of biodiesel were different from that of biodiesel, the flame penetration length values are similar at both of the temperature conditions investigated.

Figure 12 plots the flame structure in terms of mole fraction contours of several species ($O_2$, OH, CO, and $C_2H_2$) for diesel and biodiesel fuels at 3 ms from SOI. As indicated earlier (cf. Figure 7), the flame is stabilized in a fuel-rich zone at 2 ms from SOI and plotted in context of Figures 2b and 5. The fuel is completely consumed in the rich premixed reaction zone (RPZ), producing intermediate fuels, such as CO, $H_2$ (not shown here), and $C_2H_2$. These fuel species are then consumed through a diffusion-controlled combustion process in the non-premixed zone (NPZ). The OH contours confirm the double-flame structure, with negligible OH in the RPZ because of the rich mixture in this region for both of the fuels. Thus, the OH contours locate the diffusion flame region, which is consistent with the observation by Dec.[60] Furthermore, the $C_2H_2$ and CO contours indicate that most of the soot would be produced in the region downstream of the RPZ for both of the fuels, while most of $NO_x$ will be produced in the NPZ, which has the highest temperature. These contours clearly depict a partially premixed flame containing the RPZ near the flame stabilization region and the NPZ around the flame periphery for both diesel and biodiesel. Thus, the simulations are able to reproduce the "conceptual model" by Dec,[60] characterizing diesel engine combustion. Other salient differences in the flame structure of these fuels are summarized as follows: (1) The $O_2$ mole fraction contours are broader for diesel, which further indicates more ambient air entrainment and spray breakup. As explained earlier, the stoichiometric surface is further away from the spray axis for diesel, which results in broader $O_2$ mole fractions. (2) Higher OH concentrations of diesel are also observed, reflecting higher flame reactivity. The OH contours also capture the fact that biodiesel predicts higher lift-off length than diesel fuel. (3) A lower CO concentration for biodiesel is due to two reasons: (a) the amount of evaporation was lesser for biodiesel compared to diesel, and (b) there was a higher oxygen concentration in the fuel. (4) Because $C_2H_2$ is a precursor for soot formation, a lower $C_2H_2$ concentration for biodiesel indicates that the amount of soot formation may also be lower for this fuel.

**3.4. Emission Characteristics.** Figure 13 plots the heat-release rate and emission characteristics of diesel and biodiesel fuels. The heat-release rate and maximum temperatures inside the constant volume combustion chamber are higher for diesel because of two main reasons: (1) The energy content is higher for diesel compared to biodiesel. (2) The amount of fuel injected was about 10% more for diesel compared to biodiesel. However, the premix heat-release rate of biodiesel was higher because of the oxygen in the fuel, which resulted in more complete premixed-phase combustion.

Figure 13b presents volume-averaged $NO_x$ and soot concentrations versus time for the two fuels. The values are first normalized by the total amount of fuel injected for each fuel. These values were further normalized using the maximum soot and $NO_x$ values (which were observed for diesel fuel). Results do not indicate the classical trade-off between $NO_x$ and soot concentrations, because biodiesel predicts both lower $NO_x$ and soot emissions. In general, it is agreed upon that the lower soot for biodiesel is due to the fuel-bound oxygen, which oxidizes the soot produced. Another reason for lower soot concentrations could be due to lower equivalence ratios at flame lift-off length. It has been shown previously that soot production decreases if the equivalence ratio at lift-off position is closer to stoichiometric,[17,18] which is the case for biodiesel (cf. Figure 7b). While the lower soot production with biodiesel is consistent with published results in the literature, the lower $NO_x$ emission warrants further investigation. Because $NO_x$ is produced at the diffusion flame, lower flame temperatures for biodiesel (cf. Figure 13a) during the diffusion-burn period may be the main reason for $NO_x$ reduction.

To further investigate the $NO_x$ emission characteristics of both these fuels devoid of spray, mixing, and engine effects, counterflow 1D flame simulations (OPPDIF) were performed

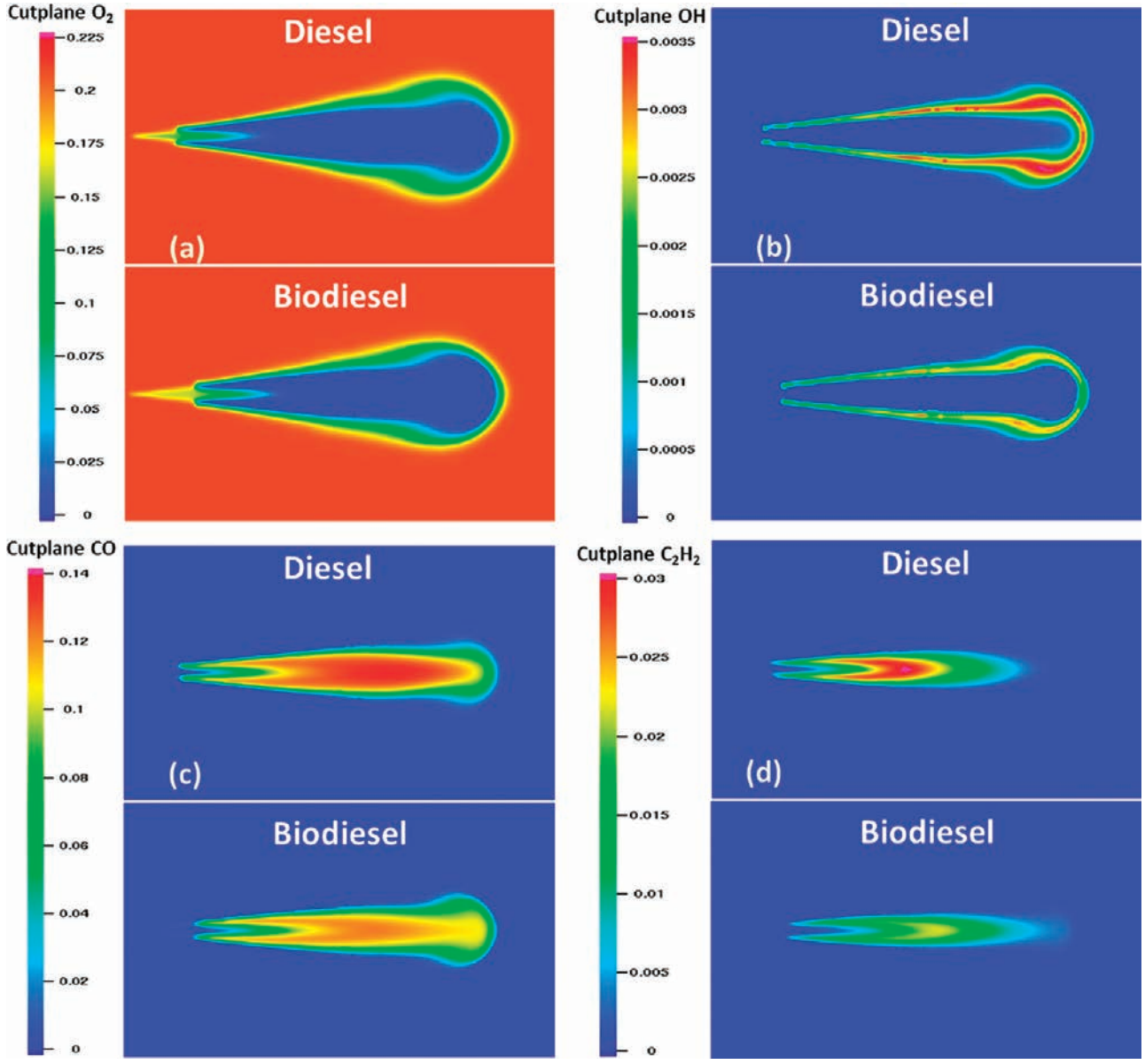


**Figure 12.** Comparison of the flame structures computed for diesel and biodiesel surrogates. The flame structure is shown at 2 ms after SOI for the base case in terms of contours of (a) $O_2$, (b) OH, (c) CO, and (d) $C_2H_2$ mole fractions.

(cf. Figure 14) using the CHEMKIN package. The flame configuration consists of two opposing jets issuing from two coaxial nozzles that are placed one above the other. Fuel (diesel or biodiesel surrogate) flows from the lower nozzle, and air flows from the upper nozzle. The diffusion flame is established under atmospheric conditions, and the temperature of the fuel and oxidizer jets is set at 300 K. Because $NO_x$ is mainly produced in the diffusion flame region, this simplified flame configuration can provide further insight into the $NO_x$ emission characteristics of these fuels. The global strain rate[61] is expressed as

$$a_s = (2|V_{ox}|/L)\{1 + |V_{fuel}|\sqrt{\rho_{fuel}}/|V_{ox}|\sqrt{\rho_{ox}}\} \quad (8)$$

where $L$ (=2 cm) denotes the separation distance between the two jets, $V_{ox}$ denotes the oxidizer jet inlet velocity, $V_{fuel}$ denotes the fuel jet inlet velocity, and $\rho_{fuel}$ and $\rho_{ox}$ denote the densities of the fuel and oxidizer streams, respectively. In a heavy-duty CI engine,[32] $NO_x$ production typically occurs during a crank angle duration of 40° for an engine speed of 1600 rpm, which results in a residence time of about 4.2 ms. OPPDIF simulations were performed with a similar residence time, resulting in a strain rate of 240 $s^{-1}$.

Figure 15 plots the $NO_x$ mole fractions under conditions mentioned in the previous paragraph with diesel and biodiesel surrogates. To identify the relative importance of different $NO_x$ formation routes, the reactions responsible for $NO_x$ formation by the other routes were suppressed. Hence, the thermal $NO_x$ values were calculated by suppressing the prompt and $N_2O$ mechanism reactions. The $NO_x$ produced with the $N_2O$ route were observed to be negligible under all conditions investigated; hence, they were not reported. The single peak in $NO_x$ values locates the diffusion flame region for both of the fuels. Thermal $NO_x$ production is significantly higher for both of the fuels compared to prompt $NO_x$. Higher thermal $NO_x$ (and hence total $NO_x$) for

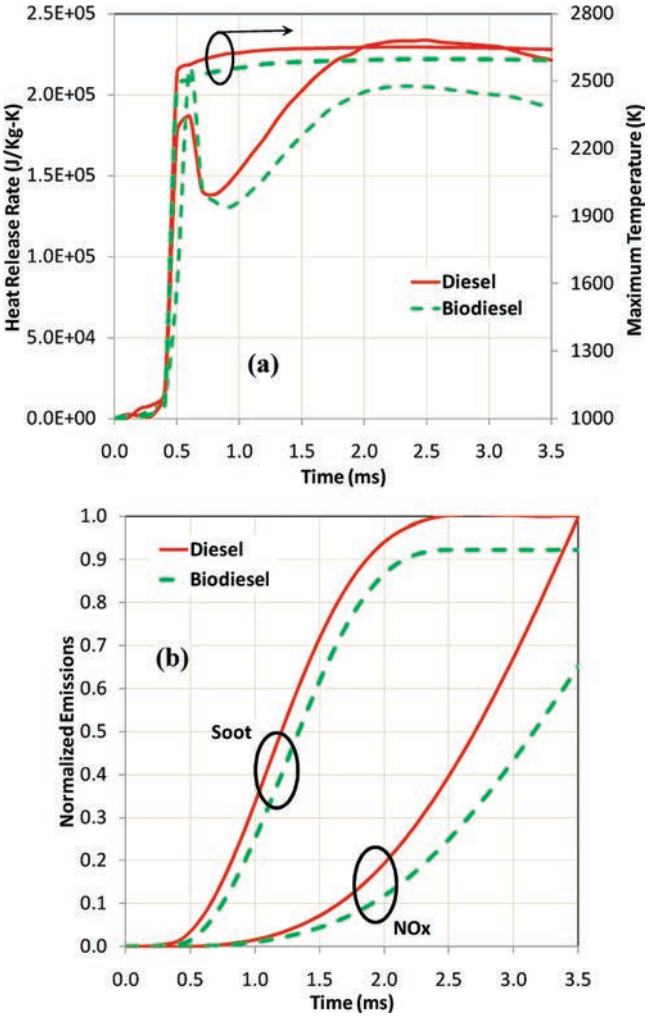


**Figure 13.** (a) Heat-release rate and maximum combustion temperatures. (b) Normalized $NO_x$ and soot emissions, for diesel and biodiesel fuels reported in the context of Figures 6 and 8 and tabulated in Table 2.

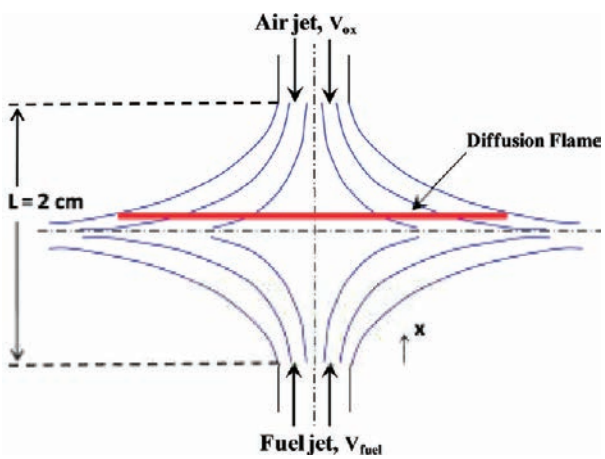


**Figure 14.** Schematic of the 1D counterflow flame configuration used in the present study to analyze $NO_x$ formation. Fuel and oxidizer nozzles along with an approximate location of the diffusion flame are also shown.

diesel surrogate fuel is due to the fact that the flame temperatures (not shown here) were also higher compared to the biodiesel

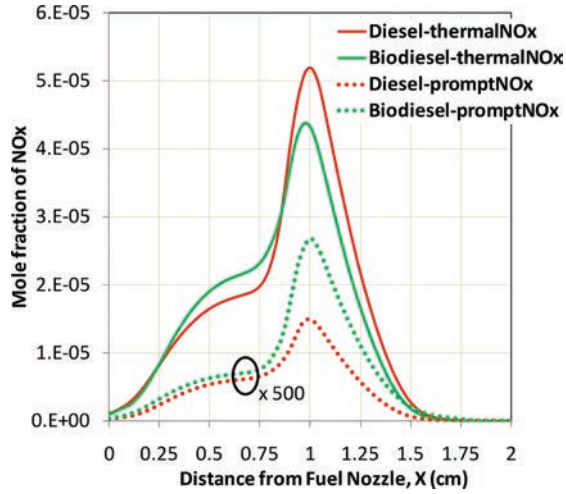


**Figure 15.** Mole fraction of thermal and prompt $NO_x$ versus distance from the fuel nozzle for diesel and biodiesel fuels.

surrogate. However, prompt $NO_x$ is observed to be higher for the biodiesel surrogate because of higher concentrations of CH and HCN (not shown here) compared to the diesel surrogate. Clearly, there are chemical kinetic reasons for higher $NO_x$ production for diesel fuel (cf. Figure 13b) in the current study. Although the biodiesel surrogate predicts higher prompt $NO_x$ values, the total $NO_x$ (thermal + prompt) does not agree with the trends reported in the literature.

Hence, our future work will focus on the development of improved chemical kinetic models for diesel and biodiesel fuels. A chemical kinetic model for a mixture of methyl decanoate, methyl decenoate, and NHPT has already been developed by our group,[53] and it is able to capture the ignition and flame characteristics at high temperatures very well. Low-temperature chemical kinetic pathways will be added to this mechanism for CI engine applications.

## 4. CONCLUSIONS

A computational study was performed to investigate the combustion and emission behavior of biodiesel and diesel fuels. The first step was to validate the detailed chemical kinetic models for the diesel and biodiesel surrogates. While NHPT, which was used as a surrogate for diesel fuel, was able to reproduce chemical ignition delay data very well, there was notable disagreement between the simulated and measured ignition delay times for the MB + NHPT mixture (which was used as a biodiesel surrogate). Three-dimensional turbulent combustion simulations in a constant volume combustion chamber were performed to validate liquid length and flame lift-off characteristics of diesel and biodiesel against data available in the literature. Ignition was seen to occur in rich mixtures for both diesel and biodiesel. It was concluded that both NHPT and MB may not be good fuel surrogates, especially at lower temperatures, because they are not able to reproduce the cetane number characteristics reported in the literature.

The liquid length was always observed to be higher than the lift-off length for biodiesel, which indicated significant interplay between spray and combustion processes, which was not the case with diesel fuel under conditions investigated. Turbulent burning velocities were calculated for both of the fuel surrogates, and it was concluded that, because turbulent burning velocities were

significantly lower than the gas-phase axial velocity, upstream flame propagation may not be the mechanism for flame stabilization. In addition, local ignition upstream and separated from the high-temperature flame regions was also not observed. Successive autoignition of the fuel stream into the combustion zone seems to be the mechanism for flame stabilization. Parametric studies were performed to understand the influence of ambient conditions, such as temperature, density, and $O_2$ concentration, on flame lift-off lengths. In general, a lesser amount of ambient air entrainment was observed for biodiesel fuel. The emission characteristics of diesel and biodiesel fuels were also compared. The classical $NO_x$ and soot trade-off was not observed because both $NO_x$ and soot concentrations were lower for biodiesel. While the reduced soot emissions with biodiesel are consistent with other studies in the literature, the reduced $NO_x$ emissions are not.

## AUTHOR INFORMATION

**Corresponding Author**

*Telephone: 1-630-252-5273. Fax: 1-630-252-3443. E-mail: ssom@anl.gov.

## ACKNOWLEDGMENT

The submitted manuscript was created by UChicago Argonne, LLC, operator of Argonne National Laboratory (Argonne). Argonne, an Office of Science, U.S. Department of Energy, laboratory, is operated under Contract DE-AC02-06CH11357. The authors acknowledge Dr. Rolf Reitz and Ms. Jessica Brakora at the Engine Research Centre at University of Wisconsin, Madison, WI, for sharing the MB and ERC-Bio mechanisms used in the current study.

## REFERENCES

(1) Graboski, M. S.; McCormick, R. L. *Prog. Energy Combust. Sci.* **1998**, *24*, 125–164.

(2) Armas, O.; Hernandez, J.; Cardenas, M. *Fuel* **2006**, *85*, 2427–2438.

(3) Grimaldi, C. N.; Postrioti, L.; Battistoni, M.; Millo, F. *Proceedings of the Society of Automotive Engineers (SAE) 2002 World Congress and Exhibition*; Detroit, MI, March 2002; SAE Paper 2002-01-0865.

(4) Hashimoto, M.; Dan, T.; Asano, I.; Arakawa, T. *Proceedings of the Society of Automotive Engineers (SAE) 2002 World Congress and Exhibition*; Detroit, MI, March 2002; SAE Paper 2002-01-0867.

(5) Agarwal, D.; Sinha, S.; Agarwal, A. *Renewable Energy* **2006**, *31* (14), 2356–2369.

(6) Vaughn, T.; Hammill, M.; Harris, M.; Marchese, A. *Proceedings of the Powertrain and Fluid Systems Conference and Exhibition*; Toronto, Ontario, Canada, Oct 2006; SAE Paper 2006-01-3302.

(7) Dagaut, P.; Gail, S.; Sahasrabudhe, M. *Proc. Combust. Inst.* **2007**, *31*, 2955–2961.

(8) Dooley, S.; Curran, H. J.; Simmie, J. M. *Combust. Flame* **2008**, *153*, 2–32.

(9) Glaude, P. A.; Herbinet, O.; Bax, S.; Biet, J.; Warth, V.; Battin-Leclerc, F. *Combust. Flame* **2010**, *157* (11), 2035–2050.

(10) Bax, S.; Hakka, M. H.; Glaude, P. A.; Herbinet, O.; Battin-Leclerc, F. *Combust. Flame* **2010**, *157* (6), 1220–1229.

(11) Brakora, J. L.; Ra, Y.; Reitz, R. D.; McFarlane, J.; Law, C. S. *Proceedings of the Society of Automotive Engineers (SAE) World Congress and Exhibition*; Detroit, MI, April 2008; SAE Paper 2008-01-1378.

(12) Ra, Y.; Reitz, R. D.; McFalane, J.; Law, C. S. *Proceedings of the Society of Automotive Engineers (SAE) World Congress and Exhibition*; Detroit, MI, April 2008; SAE Paper 2008-01-1379.

(13) Golovitchev, V. I.; Yang, J. *Biotechnol. Adv.* **2009**, *27*, 641–655.

(14) Um, S.; Park, S. W. *Fuel* **2010**, *89*, 1415–1421.

(15) Siebers, D. L.; Higgins, B. *Proceedings of the Society of Automotive Engineers (SAE) 2001 World Congress*; Detroit, MI, March 2001; SAE Paper 2001-01-0530.

(16) Higgins, B.; Siebers, D. L. *Proceedings of the Society of Automotive Engineers (SAE) 2001 World Congress*; Detroit, MI, March 2001; SAE Paper 2001-01-0918.

(17) Pickett, L. M.; Siebers, D. L.; Idicheria, C. A. *Proceedings of the Powertrain and Fluid Systems Conference and Exhibition*; San Antonio, TX, Oct 2005; SAE Paper 2005-01-3843.

(18) Pickett, L. M.; Siebers, D. L. *Proc. Combust. Inst.* **2002**, *29*, 655–662.

(19) Som, S.; Aggarwal, S. K. *Combust. Flame* **2010**, *157*, 1179–1193.

(20) Canaan, R. E.; Dec, J. E.; Green, R. M. *Trans. SAE* **1998**, *107* (3), 583–602.

(21) Wu, Y.; Huang, R.; Liu, Y.; Leick, M.; Lee, C. F. *Proceedings of the Society of Automotive Engineers (SAE) 2010 World Congress and Exhibition*; Detroit, MI, April 2010; SAE Paper 2010-01-0606.

(22) Mueller, C. J.; Boehman, A. L.; Martin, G. C. *Proceedings of the Powertrains, Fuels and Lubricants Meeting*; Florence, Italy, June 2009; SAE Paper 2009-01-1792.

(23) Som, S.; Longman, D. E.; Ramirez, A. I.; Aggarwal, S. K. *Fuel* **2010**, *89*, 4014–4024.

(24) Senecal, P. K.; Pomraning, E.; Richards, K. J. *Proceedings of the Society of Automotive Engineers (SAE) 2003 World Congress and Exhibition*; Detroit, MI, March 2003; SAE Paper 2003-01-0243.

(25) Senecal, P. K.; Richards, K. J.; Pomraning, E.; Yang, T.; Dai, M. Z.; McDavid, R. M. *Proceedings of the Society of Automotive Engineers (SAE) World Congress and Exhibition*; Detroit, MI, April 2007; SAE Paper 2007-01-0159.

(26) Richards, K. J.; Senecal, P. K.; Pomraning, E. *CONVERGE (Version 1.2) Manual*; Convergent Science, Inc.: Middleton, WI, 2008.

(27) Lapuerta, M.; Armas, O.; Rodriguez-Fernandez, J. *Prog. Energy Combust. Sci.* **2008**, *34*, 198–223.

(28) Kee, R. J.; Rupley, F. M.; Miller, J. A. *A Fortran Chemical Kinetics Package for the Analysis of Gas Phase Chemical Kinetics*; Sandia National Laboratories: Albuquerque, NM, 1993; Technical Report SAND89-8009B.

(29) Som, S.; Ramirez, A. I.; Hagerdorn, J.; Saveliev, A.; Aggarwal, S. K. *Fuel* **2008**, *87*, 319–334.

(30) Lutz, A. E.; Kee, R. J.; Grcar, J. F.; Rupley, F. M. *A Fortran Program for Calculating Opposed Flow Diffusion Flames*; Sandia National Laboratories: Albuquerque, NM, 1996; Technical Report SAND96-8243.

(31) Miers, S. A.; Kastengren, A. L.; El-Hannouny, E. M.; Longman, D. E. *Proceedings of the American Society of Mechanical Engineers (ASME) Internal Combustion Engines Division Fall Technical Conference*; Charleston, SC, Oct 2007; ASME Paper ICEF 20071735

(32) Som, S. Development and validation of spray models for investigating diesel engine combustion and emissions. Ph.D. Thesis, University of Illinois at Chicago, Chicago, IL, 2009.

(33) Som, S.; Ramirez, A. I.; Aggarwal, S. K.; Kastengren, A. L.; El-Hannouny, E. M.; Longman, D. E.; Powell, C. F.; Senecal, P. K. *Proceedings of the Society of Automotive Engineers (SAE) World Congress and Exhibition*; Detroit, MI April 2009; SAE Paper 2009-01-0838.

(34) Som, S.; Aggarwal, S. K.; El-Hannouny, E. M.; Longman, D. E. *J. Eng. Gas Turbine Power* **2010**, *132*, 1–12.

(35) Reitz, R. D. *Atomization Spray Technol.* **1987**, *3*, 309–337.

(36) Patterson, M. A.; Reitz, R. D. *Proceedings of the International Congress and Exposition*; Detroit, MI, Feb 1998; SAE Paper 980131.

(37) Schmidt, D. P.; Rutland, C. J. *J. Comput. Phys.* **2000**, *164*, 62–80.

(38) Post, S. L.; Abraham, J. *Int. J. Multiphase Flow* **2002**, *28*, 997–1019.

(39) Liu, A. B.; Mather, D. K.; Reitz, R. D. *Proceedings of the International Congress and Exposition*; Detroit, MI, March 1993; SAE Paper 930072.

(40) http://www.tfd.chalmers.se/~valeri/MECH.html.

(41) Yoshikawa, T.; Reitz, R. D. *SAE Int. J. Engines* **2009**, *1* (1), 1105–1117.

(42) Smith, G. P.; Golden, D. M.; Frenklach, M.; Moriarty, N. W.; Eiteneer, B.; Goldenberg, M.; Bowman, C. T.; Hanson, R. K.; Song, S.; Gardiner, W. C., Jr.; Lissianski, V. V.; Qin, Z. *GRI Mech-3.0*; http://www.me.berkeley.edu/gri-mech/.

(43) Som, S. A Numerical investigation of methane air partially premixed flames at elevated pressures. M.S. Thesis, University of Illinois at Chicago, Chicago, IL, Oct 2005.

(44) Miller, J. A.; Bowman, C. T. *Prog. Energy Combust. Sci.* **1989**, *15*, 287–338.

(45) Warnatz, J.; Maas, U.; Dibble, R. W. *Combustion*; Springer-Verlag: New York, 2006.

(46) Som, S.; Aggarwal, S. K. *Atomization Sprays* **2009**, *19* (9), 885–903.

(47) Abani, N.; Munnannur, A.; Reitz, R. D. *J. Eng. Gas Turbines Power* **2008**, *130*, 1–9.

(48) Beale, J. C.; Reitz, R. D. *Atomization Sprays* **1999**, *9*, 623–650.

(49) Kong, S. C.; Sun, Y.; Reitz, R. D. *J. Eng. Gas Turbines Power* **2007**, *129*, 245–251.

(50) Higgins, B. S.; Mueller, C. J.; Siebers, D. L. *Proceedings of the International Congress and Exposition*; Detroit, MI, March 1999; SAE Paper 1999-01-0519.

(51) Siebers, D. L. *Proceedings of the International Congress and Exposition*; Detroit, MI, Feb 1998; SAE Paper 980809.

(52) Mueller, C. J. *Proceedings of the Powertrain and Fluid Systems Conference and Exhibition*; San Antonio, TX, Oct 2005; SAE Paper 2005-01-3705.

(53) Luo, Z.; Lu, T.; Maciaszek, M. J.; Som, S.; Longman, D. E. *Energy Fuels* **2010**, *24*, 6283–6293.

(54) Pickett, L. M.; Siebers, D. L. *Int. J. Engine Res.* **2005**, *7*, 103–130.

(55) Naber, J. D.; Siebers, D. L. *Proceedings of the International Congress and Exposition*; Detroit, MI, Feb 1996; SAE Paper 960034.

(56) Huang, Y.; Sung, C. J.; Eng, J. A. *Combust. Flame* **2004**, *139*, 239–251.

(57) Turns, S. R. *An Introduction to Combustion*, 2nd ed.; McGraw-Hill: New York, 2000.

(58) Peters, N. *Turbulent Combustion*; Cambridge University Press: New York, 2000.

(59) Pickett, L. M.; Kook, S.; Persson, H.; Andersson, O. *Proc. Combust. Inst.* **2009**, *32*, 2793–2800.

(60) Dec, J. E. *Proceedings of the International Congress and Exposition*; Detroit, MI, Feb 1997; SAE Paper 970873.

(61) Som, S.; Aggarwal, S. K. *Combust. Sci. Technol.* **2007**, *179*, 1085–1112.